



# Wicking through complex interfaces at interlacing yarns

Robert Fischer<sup>a,b,c,\*</sup>, Christian M. Schlepütz<sup>d</sup>, René M. Rossi<sup>b</sup>, Dominique Derome<sup>e</sup>, Jan Carmeliet<sup>c</sup>

<sup>a</sup>Laboratory of Multiscale Studies in Building Physics, Empa, Swiss Federal Laboratories for Materials Science and Technology, Überlandstrasse 129, 8600 Dübendorf, Switzerland

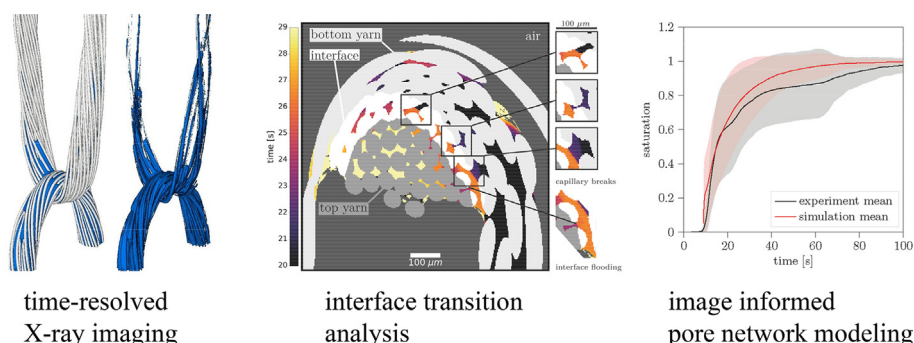
<sup>b</sup>Laboratory for Biomimetic Membranes and Textiles, Empa, Swiss Federal Laboratories for Materials Science and Technology, Lerchenfeldstrasse 5, 9014 St. Gallen, Switzerland

<sup>c</sup>Chair of Building Physics, Swiss Federal Institute of Technology Zürich (ETHZ), Stefano-Franscini-Platz 5, 8093 Zürich, Switzerland

<sup>d</sup>Swiss Light Source, Paul Scherrer Institut, 5232 Villigen PSI, Switzerland

<sup>e</sup>Department of Civil and Building Engineering, Université de Sherbrooke, J1K 2R1 Sherbrooke, Canada

## GRAPHICAL ABSTRACT



## ARTICLE INFO

### Article history:

Received 31 March 2022

Revised 16 June 2022

Accepted 21 June 2022

Available online 30 June 2022

### Keywords:

Wicking

Capillarity

X-ray tomographic microscopy

Wetting

Contact interface

Porous medium

## ABSTRACT

**Hypothesis:** Wicking flow in the wale direction of knit fabrics is slowed by capillary pressure minima during the transition at yarn contacts. The characteristic pore structure of yarns leads to an unfavorable free energy evolution and is the cause of these minima.

**Experiments:** Time-resolved synchrotron tomographic microscopy is employed to study the evolution of water configuration during wicking flow in interlacing yarns. Dynamic pore network modeling is used based on the obtained image data and distributions of delay times for pore intrusion. Good agreement is observed by comparison to the experimental data.

**Findings:** Yarn-to-yarn transition is found to coincide with slow water advance in a thin interface zone at the yarn contact. The pore spaces of the two yarns merge within this interface zone and provide a transition path. A deep capillary pressure minimum occurs while water passes through the center of the interface zone, effectively delaying the wicking flow. A pore network model considering pore intrusion delay times is expanded to include inter-yarn wicking and reproduce the observed wicking dynamics.

© 2022 The Authors. Published by Elsevier Inc. This is an open access article under the CC BY license (<http://creativecommons.org/licenses/by/4.0/>).

## 1. Introduction

Knit fabrics of interlaced yarns are used in many clothing applications with the required softness and flexibility. When in imme-

diately contact to the skin, liquid transport properties in such fabrics are important for functional clothes. Many studies have been conducted to assess the moisture management properties of a fabric, relying on an array of tests under varying conditions [1]. Wicking is the spontaneous uptake of liquid water by capillarity into a porous medium, such as textiles. Kim et al. [2] studied wicking flow in knit fabrics with water administered to one

\* Corresponding author.

E-mail address: [robert.fischer@empa.ch](mailto:robert.fischer@empa.ch) (R. Fischer).

selected yarn. Their experimental setup comprises a needle that continuously supplies liquid, mimicking closely a single sweat gland. While this method approaches a realistic textile behavior assessment, undue external pressure is imposed due to a growing drop at the needle tip. Similar limitations to the adequacy of imposed conditions can be found in Rossi *et al.* [3], where mimicking sweating from the skin through multi-layer fabrics could lead to a forced porous flow situation. In comparison, purely capillarity driven wicking is the main interest of this study. The chosen experimental method relies on an unlimited reservoir and studies short heights, allowing to neglect the effect of gravity.

Knit fabrics have two principal directions: *course* along the yarn direction and *wale* across the contacts of interlacing yarns at the knit stitches. Wicking transport occurs primarily within the yarn's pore space formed between hydrophilic fibers [4,5]. The pore space in yarns has two main directions: long and narrow pores parallel to the fibers with little change in cross-section and small contracting gaps between the fibers in the normal direction [6]. Consequently, *course* is the continuation of the fiber direction at fabric scale, taking into account the yarn meandering, while *wale* includes multiple inter-fiber gap crossings. Kim *et al.* [2] observe a preferential flow in *course* direction along the same yarn and a delay for the transfer to adjacent yarns in *wale* direction, highlighting the importance of yarn contacts in the wicking process in knit fabrics.

Observing water flow in yarns with visible light, sometimes enhanced with dyes or digital image processing, is a simple method to obtain a general understanding on the wicking dynamics. The optical method is also defined in industry standards, e.g. DIN 53924. However, due to the fiber opaqueness, visible light imaging is limited and cannot properly capture the characteristically unsaturated waterfronts in yarns [6,7]. Time-resolved X-ray tomographic microscopy (XTM) overcomes this problem and allows a precise observation of the evolution of the water configuration. XTM was already applied by the authors to study inter- and intra-fabric transport in textiles [3,8,9] and pore filling processes in yarns [6,10]. They observe irregular wicking dynamics in yarns caused by two distinct pore processes, fast pore filling and long pore-to-pore transition delays. The wicking dynamics at yarn contacts are unresolved as an additional level of multiscale complexity is created. At the pore scale, the influence of the merging intra-yarn pore structure in a complex interface zone of interlacing yarns needs to be investigated. At fabric scale, the effect of comparable yarn contacts on the wicking dynamics in the mesh of interlacing yarns in a knit fabric is not fully understood.

In the wicking process, the energy provided by wetting the solid surface is dissipated by transport of the liquid through the porous medium [11]. Transport can be described by Darcy's law:

$$p_c = RQ \quad (1)$$

where  $p_c$  [Pa] is the capillary pressure,  $Q$   $\left[\frac{m^3}{s}\right]$  the volume flux and  $R$   $\left[\frac{Pa \cdot s}{m^2}\right]$  the flow resistance. Modeling wicking uptake in yarns, however, remains challenging and not conclusively solved. Analytical models [12,13] in the Lucas-Washburn scheme [14–16] employ fit parameters and are often sufficiently suited to describe the experimental uptake curves for porous media that are effectively homogeneous macroscopically [11]. Richards' expansion [17] of Darcy's law considers unsaturated wicking uptake and has been adapted to describe wicking in certain yarns [18] and cotton fabrics [5], but is still limited to experimental fitting. Moreover, in many cases, these macroscopic models fail [4] and an alternative simple model is difficult to find. Such modeling challenges are not limited to textile wicking, but are in general relevant for two-phase flow porous media. The complexity lies in the large scale discrepancy between pore filling processes and macroscopic wicking dynamics. Spontaneous imbibition in heterogeneous porous media like yarns can

show complex dynamics because the pore scale processes directly influence the flow observed at macroscopic scale, e.g. in variable capillaries [19] or fractures [20]. Direct simulations by computational fluid dynamics (CFD) or lattice Boltzmann methods (LBM) are still computationally expensive for complex systems like yarns or even yarn interlaces. Pore network models (PNM) are an effective alternative because they can capture the macroscopic behavior by representing the porous medium as a network of pores. An essential requirement of PNMs is an accurate approximation of the pore filling processes. While the principal physics of wicking are already described, the actual structure-liquid-interactions are difficult to predict, especially for the particular pore shapes in yarns. Directly simulating the pore fillings with CFD or LBM in a coupled hybrid PNM [21–24] could present a viable option in the future, but is still too expensive to capture all fine nuances of the water evolution in the long, narrow and angular yarn pores [6]. We suggested as an intermediate step a dynamic PNM introducing time delays between pore-to-pore transitions to recover statistically the measured wicking dynamic in yarns [25]. The next step to model knit fabrics and inter-yarn wicking therefore requires a detailed understanding of the pore scale processes at the contact interface of two interlacing yarns.

Wicking across interlacing yarns can be discussed analytically for an idealized yarn interface zone (Fig. 1). Although a hexagonal lattice is the densest packing for parallel cylinders and the natural choice for an idealized structure, it cannot be used as a reference for yarns. A more open structure allows fibers to accommodate twist [12], displays inevitable randomness of fiber arrangement and leaves inter-gaps for liquid flow (Fig. 1a). As shown in the following, the most relevant feature for inter-yarn wicking is the gap between two fibers (Fig. 1b). While the wicking process in the yarns is mainly along the fiber direction, here the water in the bottom yarn must cross gaps to reach the top yarn (Fig. 1a). The water enters the hourglass shaped pore from the top and advances along  $x = r(1 - \cos \alpha)$  towards the bottom exit of the pore (Fig. 1b). The free energy  $F$  of water advancing in porous media can be written as [6,26]:

$$F = \gamma(A_{wa} - \cos \vartheta A_{ws}) \quad (2)$$

where  $\gamma$  is the surface tension of water in air,  $\vartheta$  Young's contact angle describing the water wettability of the fiber surface,  $A_{wa}$  the interface area of water and air and  $A_{ws}$  the interface area of water and solid or more simply, the wet surface.  $p_c$  is then calculated by [6]

$$p_c = -\frac{dF}{dV} = -\gamma \frac{d(A_{wa} - \cos \vartheta A_{ws})}{dV} \quad (3)$$

The water-air interface  $A_{wa}$  and wet surface  $A_{ws}$  for a given water-front position  $\alpha$  in Fig. 1b) are written with

$$A_{wa} = 2l(\Delta + r(1 - \sin \alpha)) \quad (4a)$$

$$A_{ws} = 2l\alpha r \quad (4b)$$

where  $l$  is the longitudinal dimension of the interface,  $r$  the fiber radius and  $2\Delta$  the closest distance between two fibers. A slow creeping flow from an unlimited reservoir is reasonably assumed, allowing the water-air interface to attain its minimum energy shape without volume restriction at each moment, i.e. to maintain a straight interface. The volume  $V$  is then

$$\begin{aligned} V(\alpha) &= \int_0^{x(\alpha)} A_{wa} dx = \int_0^\alpha A_{wa} r \sin \alpha d\alpha \\ &= 2lr\Delta(1 - \cos \alpha) + 2lr^2 \left(1 - \cos \alpha + \frac{\sin(2\alpha)}{4} - \frac{\alpha}{2}\right) \end{aligned} \quad (5)$$

It is found that the capillary pressure crosses zero at  $\alpha_0 = \pi - \vartheta$  and becomes negative for  $\alpha > \alpha_0$ , i.e. acting against the direction of the

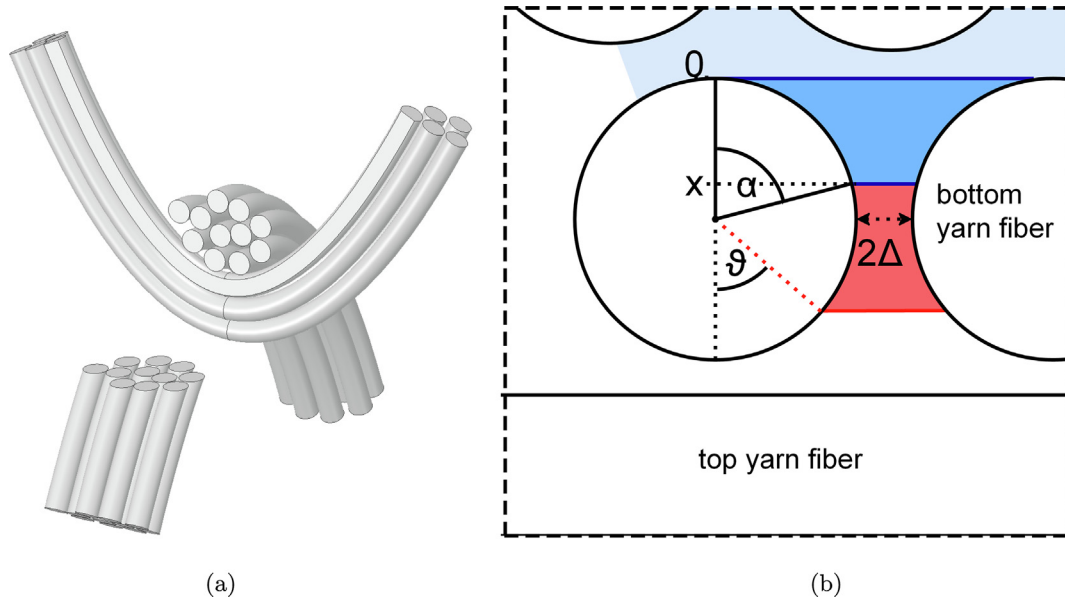


**Fig. 1.** a) Idealized pore structure of interlacing yarns. b) Schematic of water passing between fibers, in an hourglass-shaped gap, at the idealized contact zone for transition from bottom to top yarn. Light blue: initial water configuration, dark blue: differential water configuration after moving interface by  $x$ , red: change until equilibrium at free energy minimum  $\alpha_0 = \pi - \vartheta$ .

advancing interface (6a) corresponding to a free energy minimum (6b).

$$p_c = -\frac{dF}{dV} = -\frac{dF}{d\alpha} \frac{d\alpha}{dV} = 0 \quad (6a)$$

$$\frac{dF}{d\alpha} = \gamma 2l \frac{d(\Delta + r(1 - \sin \alpha) - r\alpha \cos \vartheta)}{d\alpha} = 0 \quad (6b)$$

$$\cos \alpha_0 = -\cos \vartheta \quad (6c)$$

$$\alpha_0 = \pi - \vartheta \quad (6d)$$

Without external pressure, the interface stops at this equilibrium configuration and it is then impossible for water to pass through the yarn contact of such an idealized structure. From practical and experimental observations it is clear that water can wick across yarn contacts. This means that some contact points exist between the bottom and top yarns where the capillary pressure is reduced but not attaining zero.

The aim of this study is to develop a deeper understanding of the interface wicking processes at yarn contacts in wale direction of knits. We employ synchrotron X-ray tomographic microscopy to study in detail the wicking flow in interlacing yarns. A quantitative analysis of the evolution of free energy and water configuration based on four-dimensional image data reveals a capillary minimum coinciding with the interface transition. A dynamic pore network model is employed and compared to the experimental results. We end with discussion and conclusion, including the need for further research.

## 2. Methods

### 2.1. Materials

Yarns are made from circular polyethylene terephthalate (PET) filaments with diameter of  $55 \mu\text{m}$  (3.3 tex). Surface treatment with plasma-enhanced chemical vapor deposition ensures constant and permanent water wettability with a contact angle of  $48^\circ \pm 5^\circ$  in air. The contact angle is obtained by optical measurement of a sessile drop on a flat plasma-treated PET reference piece. Bundles of 32 filaments and 0.5 m length are twisted to 200 twist per meter (tpm) under a tension of 10 mN/tex ( $\approx 14 \text{ MPa}$  for PET) using a twist tes-

ter [6]. After twisting, the yarn segments are carefully placed in frames for short (1 day) storage while maintaining tension.

As sample holder, a 10 mm Kapton tube of 35 mm length is closed by two aluminum caps that allow mounting two yarns in an interlacing configuration, mimicking to a certain degree the yarn contact of a knit stitch. Both caps have two 6 mm spaced 1 mm pinholes to receive the yarn and a base plate that can be screwed on to clamp the yarns. The top cap has a grub screw on one side that allows fixing one leg of the yarn while a weight is hung on the second leg, applying a given tension on the yarn contact, then clamping the yarn in place. Three different tensions, 2.5, 10 and 30 mN/tex are applied and five samples prepared for each tension level. The lower cap contains a wide opening acting as water inlet. This setup allows the interlacing of two yarn loops and the application of a tension at their contact while minimizing fiber rearrangements within the yarns during sample mounting as a tension is continuously maintained on the yarns. The compression, however, naturally leads to fiber rearrangement in the contact zone.

The sample assembled within the holder is then placed into the reservoir and mounted on the rotating stage of the synchrotron X-ray beamline. Illustrations of the setup are found in the supplementary material.

### 2.2. Time-resolved X-ray tomographic microscopy

Time-resolved synchrotron X-ray tomographic microscopy (XTM) is performed at the TOMCAT beamline of the Swiss Light Source, Paul Scherrer Institut, Villigen PSI, Switzerland [27]. The supplementary Table 1 contains all the important acquisition and processing parameters. Owing to the high brilliance of the X-ray source, full high-quality tomographic scans of 5.5 mm height with voxel size  $2.75 \mu\text{m}$  can be recorded at 2.5 Hz. Image acquisition starts after starting the sample rotation and remotely releasing water into the reservoir. The sample rotates at 2.5 Hz and 400 projections are recorded over every half-turn, from  $0^\circ$  to  $180^\circ$ . The second half turn is skipped and acquiring one scan takes therefore 0.2 s. The projections are Paganin filtered [28] and reconstructed [29] to yield one tomographic image every 0.4 s (2.5 Hz). After 1 min,

this rate of imaging is generally reduced to one tomographic image every 0.8 s by skipping one full turn, but variable sequences are applied in few cases.

### 2.3. Image post-processing

Our established method to segment XTM data of water-wicking yarns [6,10] is employed. The polymer phase is segmented using the Weka-plugin [30] for ImageJ/Fiji in the first, still dry, image. In the yarn contact zone, where the fibers show curved trajectories and are not always orthogonal to the xy-plane, the 3D-data is resliced in xz- and yz-planes. The 2D-based slice-wise algorithm yields more accurate results by averaging the machine learning predictions of the three orientations. After slice-wise rigid body registration, the grayscale images are masked with the previously obtained fiber phase. The remaining images require segmenting water from air, which is done by tracking the strongest grayscale gradient in time and identifying this as the appearance of water in each voxel.

The water phase in the segmented image at the end of acquisition is considered the fully saturated pore space. A restricted watershed algorithm [31] is then employed to separate the pore space into a network of connected pore bodies [6].

To label the different interlace zones, i.e. top yarn, bottom yarn and interface, the fiber extraction module in Avizo [32,33] is employed on the first dry scan to create a table containing the 64 fibers in the form of segments of connected points with floating point coordinates. The fiber segments are attributed by their mean point position to the bottom or top yarn. For each segment, the unequally spaced point coordinates are interpolated to create an integer 3D-array containing traces of connected voxels. These labeled voxel traces represented the central axis of the fibers. Assuming perfectly circular fibers, the solid phase can be reconstructed by using the Euclidean distance transform for every pixel with a value smaller than the fiber radius (10 px = 27.5  $\mu\text{m}$ ) with different labels for each fiber. From this, yarn masks are created in a two-step process. Firstly, the fibers are cleaned by slice-wise morphological closing (10 iterations) and the pore space is filled by 2D morphological hole filling. Secondly, the yarn masks are expanded by 3D morphological dilation with a ball kernel with a radius of 10 pixels. The overlap of the obtained masks is then used as definition for the interface zone at the yarn contact.  $A_{wa}$  and  $A_{ws}$  can be obtained for each time step by extracting a surface mesh of the volumetric image [6]. The free energy is calculated using the  $A_{wa}$  and  $A_{ws}$  data. The relevant image processing parameters are listed in the supplementary Table 1.

### 2.4. Network model

A pore network is created from the pores as segmented from images. We assume that the dynamics of interlaced yarns behave similar to straight yarns [6,25] as a sequence of fast pore filling events and somewhat long delays between filling events. The pore delays are determined from experiments, and their distribution is used as input to the DPNM. In an experiment, a pore filling event is defined as a flow peak with a magnitude of at least 300 voxel/s ( $\approx 6.210^{-15} \text{ mm}^3/\text{s}$ ), located at least 1 s away from the next higher peak and having a minimum prominence of 150 voxel/s ( $\approx 3.110^{-15} \text{ mm}^3/\text{s}$ ). Pore delays, or waiting times, are defined as the period between flow peaks in the combined volume flux curve of neighboring pore pairs. A pore pair is assigned to the interface if one of the two pores is at least partly in the interface zone and to the top or bottom yarn if both pores are in the respective yarns and not in the interface. Pores smaller than 100 voxels are not considered in the determination of pore delays.

The segmented image data gives the geometric information of each pore. The pores are approximated as cylindrical tubes with the radius calculated from the actual pore volume  $V_i$  and actual arc  $l_i$  length as

$$r_i = \sqrt{\frac{V_i}{\pi l_i}} \quad (7)$$

Finally, all pores that are present at the bottom of the FOV are chosen as inlets. We employ our previously developed dynamic pore network model, and we refer to our paper for more implementation details [25].

## 3. Results

Fig. 2 gives an example of the segmented images for six acquisition steps. The supplementary material contains the figure as movie (1a: wicking process showing only water, 1b: wicking process showing fibers and water) with all acquisition steps, which provide a better impression of the dynamic process.

### 3.1. General wicking dynamics

The supplementary section contains additional figures on the experimental results that are supportive but not essential for the analysis.

Of the 15 prepared samples, 12 could be processed. The remaining 3 showed either sample movement leading to image artifacts or a failed timing of releasing water to the reservoir and starting image acquisition. Fig. 3 shows the global water wicking dynamics in terms of absolute uptaken water volume. Visual inspection reveals that, with the exception of samples "30 mN/tex 3" and "30 mN/tex 4", the entire pore space is filled with water at the end of acquisition. Only a few pores in the upper yarn are filled in "30 mN/tex 3" and no water reaches the upper yarn in "30 mN/tex 4", while the lower yarns become saturated in both cases. One sample (2.5 mN/tex 3) takes up much more water than the other samples. Sample assembly has likely failed for this samples as the fibers are standing off like fuzzy hairs resulting in much larger inter-fiber pore volume compared to the other samples. Two types of uptake dynamics are observed. Six samples are filled in one instant, while the other six samples show a plateau in the uptake curve. The latter behavior is best seen in supplementary movie 1b, animating the time series in Fig. 2. After the completion of filling the bottom yarn in Fig. 2b, the water configuration remains largely in the configuration displayed in Fig. 2c before filling in the top yarn commences in Fig. 2d. This delay should be discussed. The period of the water configuration in Fig. 2c corresponds to the transition of water from the lower to the upper yarn and the plateau in the uptake curve. In the bottom yarn, the long and parallel inter-fiber pores are filled simultaneously with a comparable position of the water front in every pore. In the top yarn, water uptake happens in a sequence of pore fillings starting from pores connected to the contact interface. Because the inter-fiber yarn pores are long and narrow, water can reach the top of the field of view (FOV) much earlier than filling pores at lower heights, leading to the pattern in Fig. 2d and e. At the end of the uptake, the entire pore space inside the yarns is filled with water (Fig. 2f). The yarn pore space is the inter-fiber void space, but it is unclear from geometrical consideration alone what the boundary is to the surrounding air. Therefore, the pore space is defined as the volume occupied by water at the end of acquisition ( $t \rightarrow \infty$ ), denoting the active void space relevant for wicking. For each tomographic slice at height  $h$ , the porosity is calculated as:



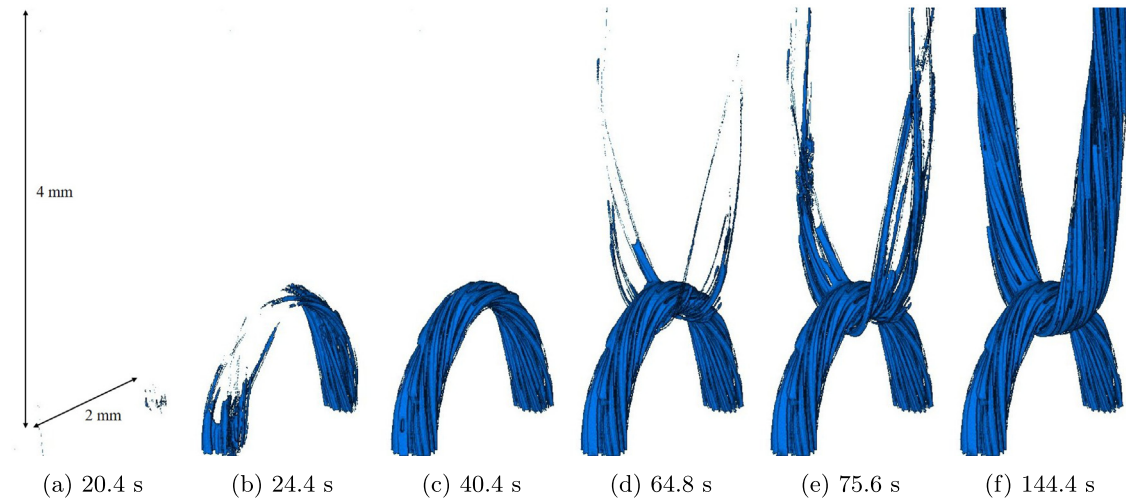


**Fig. 2.** Perspective visualization of segmented volumetric data at selected time steps with water in blue. Sample: "2.5 mN/tex 1". The distance of yarn legs is around 2 mm at the bottom and the height of the image 4 mm.

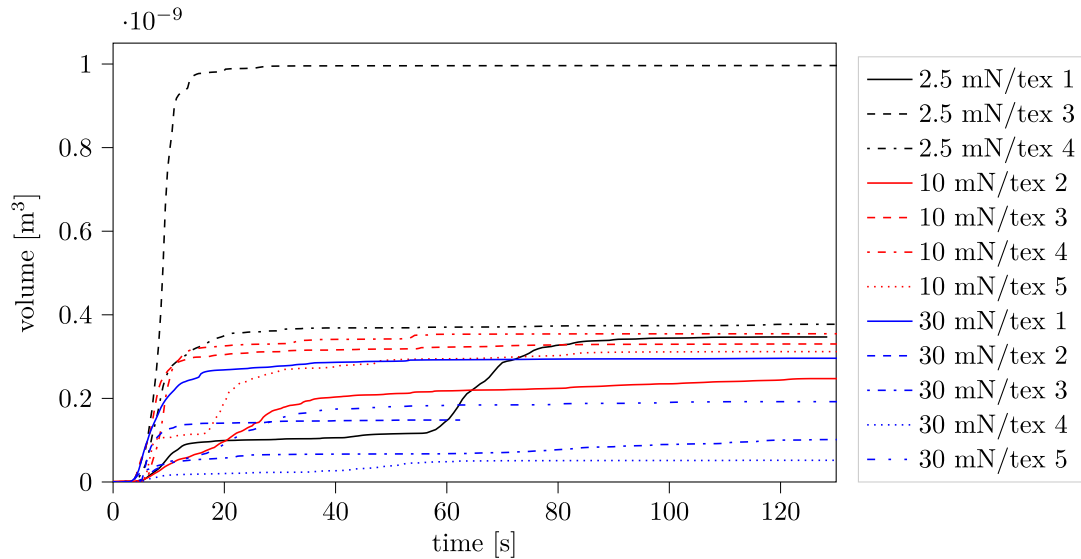


**Fig. 3.** Total water uptake over time in the FOV for all samples.

$$\text{porosity}(h) = \frac{\text{waterpixel}(h, t \rightarrow \infty)}{\text{waterpixel}(h, t \rightarrow \infty) + \text{fiberpixel}(h)} \quad (8)$$

This pore space and porosity definition is robust with the exception of the two samples not filling the entire inter-fiber space of the top yarn ("30 mN/tex 3" and "30 mN/tex 4"). The porosity profiles show a common pattern for all samples: there is a 0.5 mm high zone at the yarn contact ( $h = 0$ ) with reduced porosity compared to the rest of the sample. There might be an observable influence of applied tension on contact zone porosity due to stronger compression and also on the transition dynamics (supplementary material). However, the spread of measured values is too large and the number of repeats too small to reliably detect a clear effect of applied tension.

### 3.2. Yarn contact transition dynamics

The delay of the water transition from the bottom to the top yarn at the low porosity yarn contact zone warrants a closer examination. We define the interface delay as the time elapsed between

filling 5% of the interface zone and filling 5% of the volume of the top yarn pores. The statistical distribution of interface delays for all samples is shown in Fig. 4 and fitted to an approximated generalized Gamma distribution [6,34] also commonly used to describe the recurrence times of earthquakes.

$$F(\Delta t) = \frac{C}{\Delta t^{1-\delta}} e^{-\frac{\Delta t}{B}} \quad (9)$$

The probability  $F$  of finding a delay value of  $\Delta t$  is calculated with a scaling factor  $C$ , a shape factor  $\delta$  (typically 0.6 for earthquakes [34]) and a soft cut-off  $B$  that increasingly dampens the probability of large  $\Delta t$ . For the interface delays, the obtained fit parameters are  $\delta = 0.7$ ,  $C = 0.7 \text{ s}^{1-\delta}$  and  $B = 36.93 \text{ s}$ .

To better understand the transition process, the active pore space, i.e. the volume that displays the change of the water configuration during the transition, is displayed as an illustrative delay at such a yarn transition in Fig. 5 and compared to the process inside the interface zone. The data for the other samples are shown in the supplementary section for cases without delay and with interface delay. For the cases with interface delay, changes in water config-

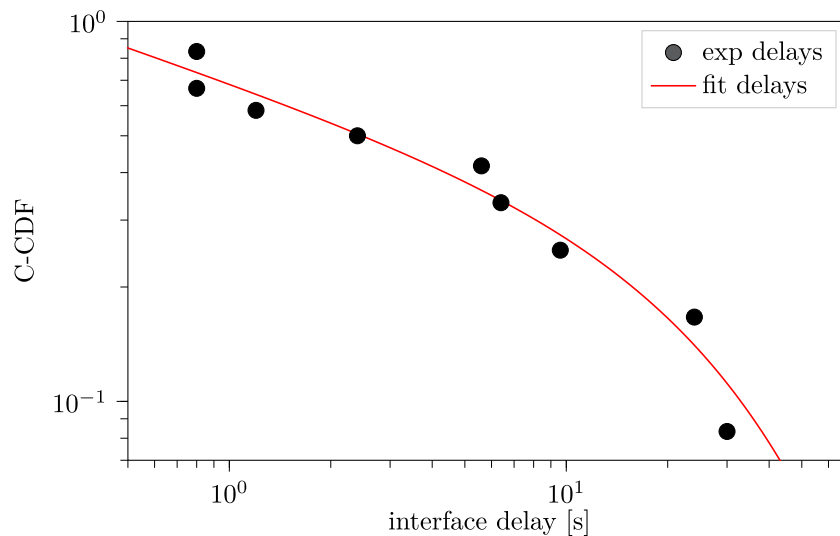


Fig. 4. Complementary cumulative distribution function for delays in black and fit of “earthquake” gamma distribution in red.

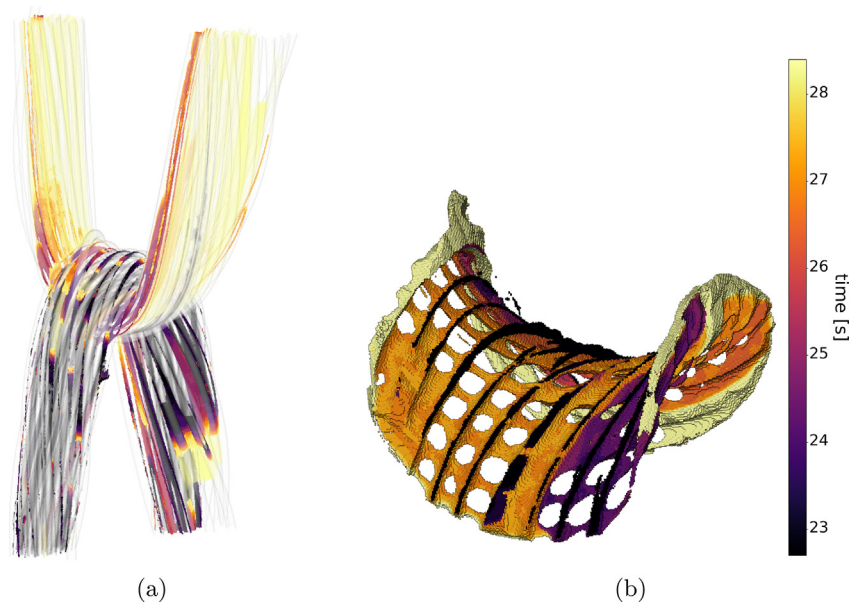
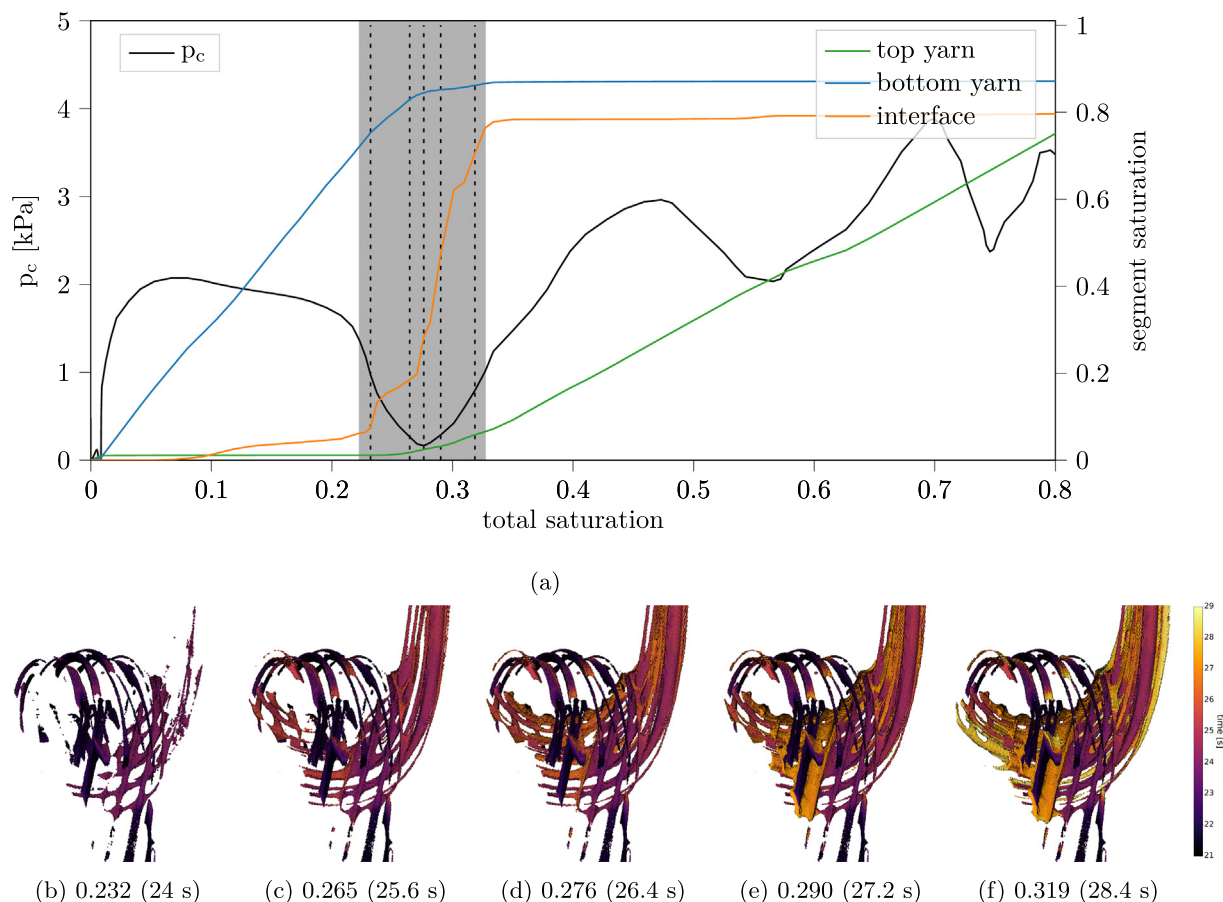


Fig. 5. a) Water configuration changes during the yarn transition delay in color for the corresponding time from 23 to 28 s. Fibers are transparent white, pore space filled before and after the delay partially transparent with color labeling. Height of the displayed region: 3 mm, yarn spacing at top: 1 mm. b) Evolution of water configuration at the interface zone. Width of displayed region: 0.5 mm ( $\approx$  yarn diameter). Sample 10 mN/tex.

uration during the delay almost exclusively occur in the interface zone, with the exception of few pores that are connected to the interface zone (Fig. 5) and the interface undergoes filling only during the interface delay (Fig. 5). The pore space at the interface has an almost regular waffle structure that is bent into a saddle, a shape produced by the two orthogonally stacked parallel fiber arrays at the yarn contact (Fig. 5b). In cases with delays, the transition of this interface happens only at one observable location in the waffle-like pore space. The cases without delay have no indication of such a single localization of the water crossing the interface since the process is too fast to be documented with the temporal resolution. The data provide no direct explanation why some samples show interface delays. All samples display the same visual characteristics and dimensions.

The high temporal resolution data obtained provides all the information necessary for the capillary pressure to be calculated

at each time step with the Eq. (3). The water–air–interface area  $A_{wa}(t)$ , wetted solid surface area  $A_{ws}(t)$  and filled volume  $V(t)$  are obtained from the image data. Because  $V$  increases monotonically with  $t$ , we can calculate the gradient  $\frac{dF}{dV}$  from the free energy  $F(V)$  as a function of the volume  $V$ . The obtained numeric gradient is then low-pass filtered to remove noise. Fig. 6 contains the evolution of the saturation of the bottom yarn, top yarn and interface over the total sample saturation, which increases monotonically with time, and compares it to the capillary pressure at each saturation state. Saturation is defined as the fraction of water volume compared to water volume at the end of acquisition. The discrimination in two types of uptake dynamics, also holds here. In the cases with transition delay (Fig. 6 and supplementary material), uptake in the lower yarn is completed before water flows substantially in the upper yarn. While small changes of water configuration in the bottom yarn are still observed towards the end of



**Fig. 6.** a) Capillary pressure versus total sample saturation and the saturation in the different zones vs. the total saturation for sample 10 mN/tex 2. The gray area denotes the interface delay period. b-f) Series of images of the water filling during interface delay for the five saturation levels marked by dashed lines in a).

acquisition, saturation in the bottom yarn has reached 80% before top yarn saturation passes 10%.

There is one clear global minimum of  $p_c$  that occurs in the period when the interface zone is filled during the transition delay (Fig. 6). Moreover, the capillary pressure minimum coincides with the interface region reaching 50% saturation. The onset of the filling in the top yarn occurs after the  $p_c$ -minimum followed by an increase of  $p_c$  back to the average level. The temporal median, defined for the periods outside the interface delay, of the capillary pressure  $p_c$  shows a value of around 2.5 kPa for all samples.

The samples without transition delay present a different picture. Uptake in the top yarn already takes up water before the bottom yarn is saturated (supplementary material). The capillary pressure remains at comparable levels throughout the process and no real minimum in  $p_c$  is present.

Fig. 6b-f highlights the interface transition in sample "10 mN/tex 2" focused on a region of interest where the transition occurs. Colors indicate the evolution of the water configuration. Water appearing before  $t = 21$  s is masked. The "active" water during the interface delay is shown in Fig. 5 and the full process is found as video in the supplementary movie 2.

The corresponding saturation of the bottom yarn, the top yarn and the interface are plotted together with the capillary pressure over time in Fig. 6. Prior to the transition, water is rising in pores of the bottom yarn (total saturation ( $ts$ ) < 0.23,  $t$  < 24 s). Once the water in these pores reaches the interface zone ( $ts = 0.23$ ,  $t = 24$  s), the capillary pressure  $p_c$  decreases strongly, but remains positive. Connected pores of the top yarn are filled in the interface zone, but also at some distance from the contact

(Fig. 6c,d). These first fillings in the top yarn are not yet sufficient to instigate the top yarn uptake process. At this point, the filled pore spaces in the interface are hard to attribute to either of the two yarns and belong to the complex interface at the contact of the two yarns. The crucial moment happens just before  $t = 27.2$  s (Fig. 6e), when a large portion of this merging pore space gets filled, referred to as interface flooding in Fig. 7.  $p_c$  re-surges and the entire interface region is flooded rapidly, thus previously immobile interfaces are mobilized (Fig. 7 "interface flooding" and Fig. 6e,f). From then, the pore space in the top yarn is connected to the interface and eventually the entire top yarn gets filled. Fig. 7 is an illustrative cut of the same data in the longitudinal direction.

It is also interesting to estimate the average flow resistance during the wicking process, as this image data allows to calculate this information. The flow resistance  $R$  is estimated with Eqs. (1) and (3)

$$R = - \left( \frac{df}{dV} \right) \left( \frac{dV}{dt} \right) \quad (10)$$

$R$  shows little variance during the interface transition (supplementary material). This means that the main reason for the interface delay is a minimum in capillary pressure and not an increase in flow resistance.

### 3.3. Pore transition delays and network model

Wicking delays are not only observed between yarns, but also as delays between pore filling events [6]. The experimental pore

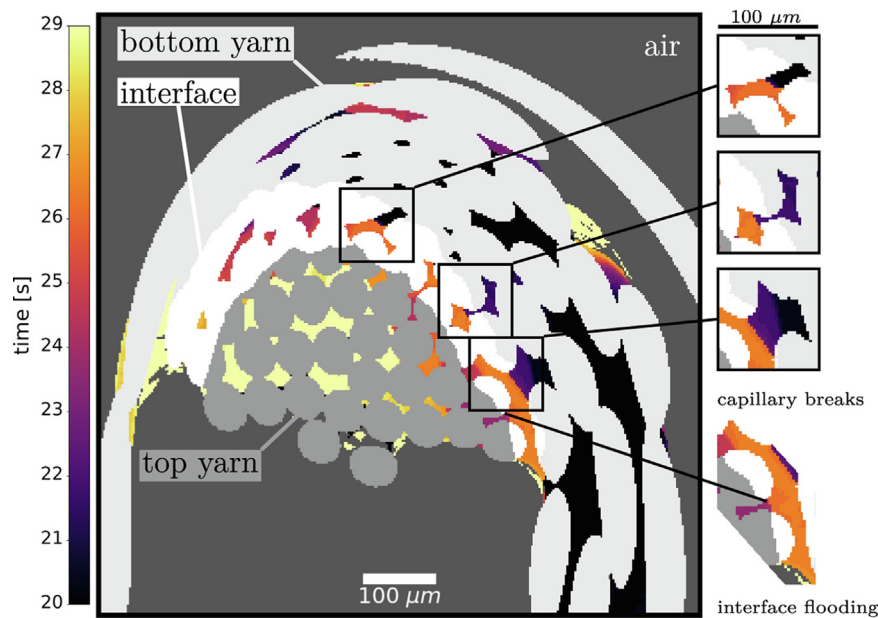


Fig. 7. Selected tomographic slice showing the water configuration changes during the yarn transition delay in color for the time.

delay distributions for bottom yarn, top yarn and interface can be fitted to the same modified generalized Gamma distribution as the interface delays with the same shape factor of around 0.7 as before, but different scaling and cut-off. Effectively, for the dynamic pore network model (DPNM), a pore delay is picked from the distribution for each pore connection. Depending on the position of the connection in the pore network, the pore delay can have a strong impact on the overall dynamics. The supplementary material contains supportive figures to illustrate the model implementation and the fit parameters. Using the different networks, 124 simulation runs are performed and the results are plotted as saturation versus time in Fig. 8. The same data is additionally displayed as absolute volume uptake and moisture content in the supplementary material. Samples "2.5 mN/tex 3" and "30 mN/tex 4", which are the outlier and the sample that does not fill the top yarn, are

excluded, because the empirical top yarn waiting times and network structure are missing. The mean uptake curve and the corresponding variance show good agreement. In addition, a varying random interface delay is recovered for most samples. The characteristic range of experimental uptake dynamics where some samples show long interface delays is also found for several simulation runs, though not necessarily for the same samples. The sample "2.5 mN/tex 1" with a pronounced experimental delay shows only short delays in all simulation runs.

#### 4. Discussion

The experimental data shows two regimes for inter-yarn wicking, without and with delay at the yarn contact transition. The latter occurs together with a deep minimum of capillary pressure  $p_c$ .

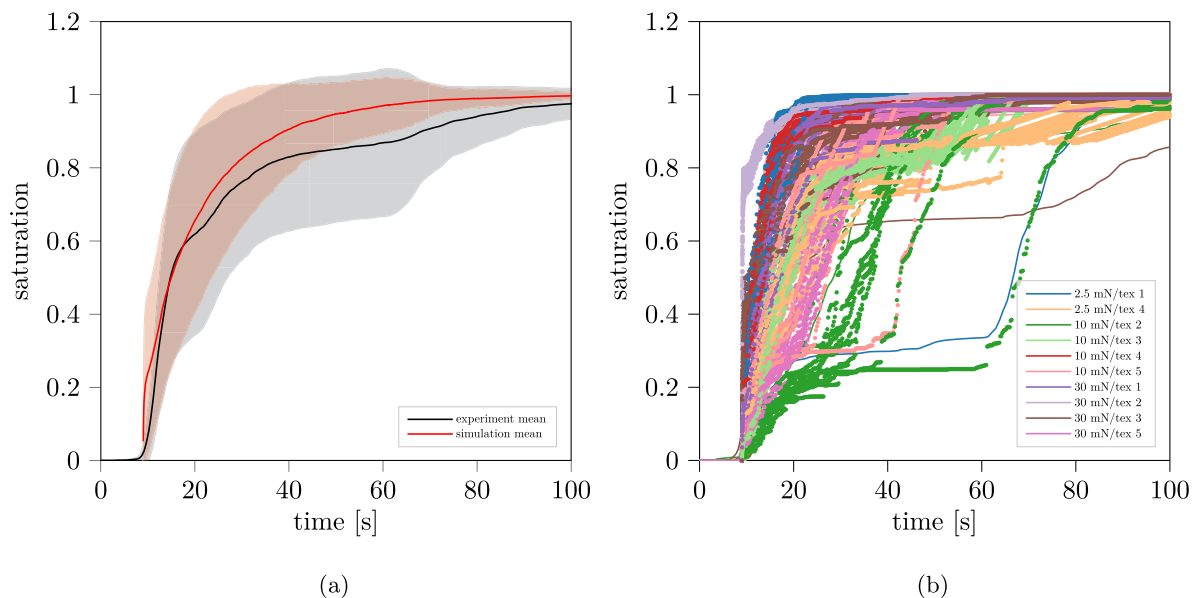


Fig. 8. a) mean uptake curves with standard deviation (light area) for all experiments (black) and simulations (red). b) Experimental uptakes as solid lines and simulation runs dotted in same color for each sample.



The  $p_c$  minimum at the yarn contact boundary, causing an interface delay for wicking, is shown to be of geometric origin due to an unfavorable free energy evolution for water passing through inter-fiber gaps. Considering an ideal contact of interlacing yarns (Fig. 1b) water transition would be entirely prevented because of an unfavorable evolution of free energy. The real, observed porous structure at the yarn contact deviates, however, from the ideal structure (Fig. 1). Fig. 7 gives an exemplary tomographic slice of such a real interface zone, where the temporal evolution of the water configuration is shown in color. The locations marked as "capillary breaks" at the interface boundary (bright white fibers) are similar to the inter-fiber gap described in Fig. 1. The predicted stabilization of the water configuration for such a geometry is observed experimentally. Originating from the pore space of the bottom yarn (light gray), water advances until a short distance from the narrowest fiber spacing and the remaining pore space is only filled a few seconds later, as shown by the clear change of color from dark violet to orange. However, the interface does not re-mobilize after this delay. The adjacent pore space is instead filled via an advancing interface from pores in the top yarn (dark gray), marked as "interface flooding". The color change from purple to orange shows that water has been already present in the top yarn before the interface zone is filled. The path from bottom to top yarn happens through an interface zone whose geometry is the complex merging of the pore spaces of the respective yarns (Fig. 6). This merging created by compression at the yarn contact is a perturbation, but not a complete deviation, of the ideal structure in Fig. 1. While the water is passing through this merging zone, the capillary pressure experiences a deep minimum, which effectively slows down the wicking flow. The amount of compression appears less relevant as this behavior was observed equally for all tested tension values.

The complex yarn contact interface structure makes it currently impossible to predict the evolution of the water configuration and the corresponding  $p_c$  from the yarn structure in the same way as for the ideal structure. Nevertheless, the  $p_c$  minimum at the 50% filled interface zone and qualitative analysis of the time-resolved image data are strong indications that the interface delay is linked to an unfavorable free energy evolution at the yarn-to-yarn transition. The actual interface zone shown in Figs. 5–7 displays a high similarity to the idealized pore structure of Fig. 1 and the predicted capillary breaks at the hourglass shaped pores at fiber transitions are also observed experimentally in several locations (Fig. 7). While wicking transport across contacts of ideal yarns is impossible due to a positive free energy gradient, i.e. negative capillary pressure, yarn twist, inherently distorted fiber arrangements and contact compression, create a distorted pore merging zone at the interface. This irregular merging zone deviates enough from the ideal interface and hinders, yet not prevents, the yarn-to-yarn transition passing a capillary pressure minimum as critical transition moment. Depending on the characteristics of this minimum, wicking flow passes immediately from yarn to yarn, is delayed up to 30 s (sample "2.5 mN/tex 1") or in one case, is prevented entirely ("30 mN/tex 4").

The interface delay at yarn contacts follows a principle similar to the one previously reported for delays in pore-to-pore transitions [6] inside yarns. Due to their dependence on the complex pore structure and evolution of water configuration, it is currently not possible to predict the quasi-idle periods between pore filling events. However, it is found that yarn interface delays as well as pore delays in yarns and interlaces follow a generalized gamma distribution with a comparable shape factor. The obtained pore structure parameters, image data and pore delay distributions do not provide a conclusive explanation why equally prepared samples show interface delays only in some cases. It has been shown earlier [6,25], that pore delays at connections that are crucial for

the pore network navigability have a strong impact on the global wicking dynamics in yarns. While these pore delays are technically deterministic, they depend on subtle variations in the pore shapes and water configuration evolution and appear random, yet they follow a characteristic statistical distribution. High-quality direct numeric methods would be required to recover such deterministic behavior but are currently computationally out of reach. Given the experimentally observed widely varying macroscopic wicking dynamics, it is reasonable to combine the pore network topology with the stochastic pore scale dynamics in a dynamic pore network model (DPNM) using the pore delay time distribution as input. Our model is able to reproduce the mean curve and also the statistical variance of the water uptake. Individual simulation runs display behavior both qualitatively and quantitatively comparable to that captured in experimental runs. In several cases, fast filling of bottom and top yarns is observed with varying interface delays, covering the same range as experimentally observed. After the yarn transition, water uptake recovers to pre-transition flow rates in both experiment and simulation (slopes in Fig. 3 and Fig. 8b), ruling out strong influences of resistances present in the interface zone. This is also shown by the estimation of flow resistance from the image data, where no clear increase in resistance is observed during the wicking process. The described transition delay can explain the different wicking dynamics in course (along the same yarn) and wale (across yarn contacts) in knit fabrics while the local yarn dynamics do not differ after the contact transition [35]. As a practical implication for the development of wicking-enhancing fabrics, irregular pore structures should be preferred and yarns with equally sized circular filaments, like the presented material should be avoided. Profiled fibers [36] and mixed fiber sizes [37] can help to create disordered contact zones and better merge pore spaces to prevent a similar  $p_c$  minimum. Increasing the number of fibers in yarns would also improve the probability of path finding across the interface. Lowering the contact angle shrinks the zone of negative capillary pressure for the ideal interface structure (Fig. 1) and can lower the requirement for pore space merging to improve wicking beyond the obvious effect of overall enhancing wicking transport.

## 5. Conclusion

We employ time-resolved X-ray tomographic microscopy (XTM) to study wicking flow across interlacing yarn contacts with similar characteristics as those in knit stitches. XTM reveals the pore structure of the yarns and the interface zone at the yarn contact. More importantly, the evolution of the water configuration can be observed with high temporal and spatial accuracy. To the best of our knowledge, wicking flow across yarn contacts has not been studied before in the same detail, especially with attention to the possibility of long delays for wicking flow across yarns. Irregular wicking transport in textiles has been described before [7,35,16], but has not been conclusively explained and has been attributed to varying pore sizes without further explanation. Our study presents an alternative to extensive parametric sweeping and fit parameter collection by studying in detail the underlying principles of wicking at yarn contacts as important feature of knit fabrics. Employing XTM, we find that the interface delays are caused by a pore structure induced minimum of the capillary pressure at a thin interface zone where the pore spaces of two yarns merge. The minimum emerges at the widening of the pore space after passing through the gap between two fibers. Creating an additional water-interface area has to be paid off by wetting a solid surface, explaining a minimum in capillary pressure. This relation between free energy and capillary pressure has received little attention in porous media research [26], but could help to better

understand pore scale two-phase flow dynamics in general. From earlier studies [6,25] on yarns, we have learned that similar capillary pressure minima also exist at pore-to-pore transitions. We exploit this behavior to extend our dynamic pore network model (DPNM) developed earlier for yarns [25] to interlaces. A pore network is extracted from the image data and a random pore intrusion delay is assigned to each pore connection according to the empirical pore delay distribution of the corresponding yarn zone to approximate the dynamics of intra- and inter-yarn pore transitions. The DPNM can stochastically reproduce the general wicking dynamics, including the interface delay, mean and variance of the uptake. Due to the chaotic and stochastic fiber arrangement in yarns, interface delays show high variance among equally prepared samples and eludes direct prediction of the wicking dynamics.

Future research can include the extrapolation of the model to connected yarn interlaces that is then compared with experimental macroscopic wicking dynamics in knit fabrics. Coupling the DPNM to direct pore simulations [21–24] can replace the experimental input of pore delay distribution and enhance the applicability of the model to deterministic wicking prediction.

### Declaration of Competing Interest

The authors declare that they have no known competing financial interests or personal relationships that could have appeared to influence the work reported in this paper.

### Acknowledgments

We are grateful to Monosuisse AG for providing the fibers and Dirk Hegemann for the fiber surface treatment with PECVD. We gratefully acknowledge Stefan Kunz for the help with the experimental setup based on a design of Sascha Krügl and Stefan Kunz. We also want to thank Sascha Krügl, Mathieu Decrette and Marie-Ange Bueno for the support during the sample preparation. We further acknowledge the Paul Scherrer Institut, Villigen, Switzerland for provision of synchrotron radiation beamtime at the TOMCAT beamline X02DA of the SLS. This research did not receive any specific grant from funding agencies in the public, commercial, or not-for-profit sectors.

### Appendix A. Supplementary material

Supplementary data associated with this article can be found, in the online version, at <https://doi.org/10.1016/j.jcis.2022.06.103>.

### References

- [1] M. Parada, D. Derome, R.M. Rossi, J. Carmeliet, *Text. Res. J.* 87 (1) (2017) 110, <https://doi.org/10.1177/0040517515622151>.
- [2] H.s. Kim, S. Michielsen, E. DenHartog, *Colloids Surf., A* 622 (2021), <https://doi.org/10.1016/j.colsurfa.2021.126726>.
- [3] R.M. Rossi, R. Stämpfli, A. Psikuta, I. Rechsteiner, P.A. Brühwiler, *Text. Res. J.* 81 (15) (2011) 1549, <https://doi.org/10.1177/0040517511413317>.
- [4] M. Parada, P. Vontobel, R.M. Rossi, D. Derome, J. Carmeliet, *Transp. Porous Media* 119 (3) (2017) 611, <https://doi.org/10.1007/s11242-017-0901-5>.
- [5] M. Parada, X. Zhou, D. Derome, R.M. Rossi, J. Carmeliet, *Text. Res. J.* (2018), <https://doi.org/10.1177/0040517518758007>.
- [6] R. Fischer, C.M. Schlepütz, D. Hegemann, R.M. Rossi, D. Derome, J. Carmeliet, *Phys. Rev. E* 103 (2021) 5, <https://doi.org/10.1103/PhysRevE.103.053101>.
- [7] A.B. Nyoni, D. Brook, *J. Text. Inst.* 97 (2) (2006) 119, <https://doi.org/10.1533/joti.2005.0128>.
- [8] P. Birrfelder, M. Dorrestijn, C. Roth, R.M. Rossi, *Text. Res. J.* 83 (14) (2013) 1477, <https://doi.org/10.1177/0040517512460296>.
- [9] G. Zhang, R. Parwani, C.A. Stone, A.H. Barber, L. Botto, *Langmuir* 33 (43) (2017) 12072, <https://doi.org/10.1021/acs.langmuir.7b02982>.
- [10] M.Y.I. Parada, C.M. Schlepütz, R.M. Rossi, D. Derome, J. Carmeliet, *Text. Res. J.* (2019), <https://doi.org/10.1177/0040517519843461>.
- [11] P. de Gennes, F. Brochard-Wyart, D. Quere, *Capillarity and Wetting Phenomena: Drops, Bubbles, Pearls, Waves*, Springer, New York, 2013.
- [12] T. Liu, K.F. Choi, Y. Li, *J Colloid Interface Sci* 318 (1) (2008) 134, <https://doi.org/10.1016/j.jcis.2007.10.023>.
- [13] J. Cai, E. Perfect, C.L. Cheng, X. Hu, *Langmuir* 30 (18) (2014) 5142, <https://doi.org/10.1021/la5007204>.
- [14] R. Lucas, *Kolloid-Zeitschrift* 23 (1) (1918) 15, <https://doi.org/10.1007/BF01461107>.
- [15] E.W. Washburn, *Phys. Rev.* 17 (3) (1921) 273, <https://doi.org/10.1103/PhysRev.17.273>.
- [16] E. Kissa, *Text. Res. J.* 66 (10) (1996) 660, <https://doi.org/10.1177/004051759606601008>.
- [17] L.A. Richards, *Physics* 1 (5) (1931) 318, <https://doi.org/10.1063/1.1745010>.
- [18] M.A.F. Zarandi, K.M. Pillai, *AIChE J.* 64 (1) (2018) 306, <https://doi.org/10.1002/aic.15856>.
- [19] D. Patro, S. Bhattacharyya, V. Jayaram, *J. Am. Ceram. Soc.* 90 (10) (2007) 3040, <https://doi.org/10.1111/j.1551-2916.2007.01776.x>.
- [20] S. Roels, K. Vandersteen, J. Carmeliet, *Adv. Water Resour.* 26 (3) (2003) 237, [https://doi.org/10.1016/s0309-1708\(02\)00185-9](https://doi.org/10.1016/s0309-1708(02)00185-9).
- [21] X. Miao, K.M. Gerke, T.O. Sizonenko, *Adv. Water Resour.* 105 (2017) 162, <https://doi.org/10.1016/j.advwatres.2017.04.021>.
- [22] A. Rabbani, M. Babaei, *Adv. Water Resour.* 126 (2019) 116, <https://doi.org/10.1016/j.advwatres.2019.02.012>.
- [23] J. Zhao, F. Qin, D. Derome, J. Carmeliet, *J. Hydrol.* 588 (2020), <https://doi.org/10.1016/j.jhydrol.2020.125080>.
- [24] J. Zhao, F. Qin, Q. Kang, D. Derome, J. Carmeliet, *Drying Technology* pp. 1–16 (2021). DOI 10.1080/07373937.2021.1933017.
- [25] R. Fischer, C.M. Schlepütz, J. Zhao, P. Boillat, D. Hegemann, R.M. Rossi, D. Derome, J. Carmeliet, *J. Colloid Interface Sci.* 625 (2022) 1, <https://doi.org/10.1016/j.jcis.2022.04.060>.
- [26] A. Ferrari, I. Lunati, *Adv. Water Resour.* 74 (2014) 1, <https://doi.org/10.1016/j.advwatres.2014.07.009>.
- [27] U. Bonse, M. Stampanoni, A. Groso, A. Isenegger, G. Mikuljan, Q. Chen, A. Bertrand, S. Henein, R. Betemps, U. Frommherz, P. Böhler, D. Meister, M. Lange, R. Abela, *Trends in synchrotron-based tomographic imaging: the sls experience* (2006), <https://doi.org/10.1117/12.679497>.
- [28] D. Paganin, S.C. Mayo, T.E. Gureyev, P.R. Miller, S.W. Wilkins, *J. Microsc.* 206 (2002) 33, <https://doi.org/10.1046/j.1365-2818.2002.01010.x>.
- [29] F. Marone, M. Stampanoni, *J Synchrotron Radiat* 19 (Pt 6) (2012) 1029, <https://doi.org/10.1107/S0909049512032864>.
- [30] I. Arganda-Carreras, V. Kaynig, C. Rueden, K.W. Eliceiri, J. Schindelin, A. Cardona, H. Sebastian Seung, *Bioinformatics* 33 (15) (2017) 2424, <https://doi.org/10.1093/bioinformatics/btx180>.
- [31] B. Münch, P. Gasser, L. Holzer, R. Flatt, *J. Am. Ceram. Soc.* 89 (8) (2006) 2586, <https://doi.org/10.1111/j.1551-2916.2006.01121.x>.
- [32] B. Weber, G. Greenan, S. Prohaska, D. Baum, H.C. Hege, T. Muller-Reichert, A.A. Hymann, J.M. Verbavatz, *J Struct Biol* 178 (2) (2012) 129, <https://doi.org/10.1016/j.jsb.2011.12.004>.
- [33] A. Rigort, D. Gunther, R. Hegerl, D. Baum, B. Weber, S. Prohaska, O. Medalia, W. Baumeister, H.C. Hege, *J Struct Biol* 177 (1) (2012) 135, <https://doi.org/10.1016/j.jsb.2011.08.012>.
- [34] A. Corral, *Phys Rev Lett* 92 (10) (2004) 108501, <https://doi.org/10.1103/PhysRevLett.92.108501>.
- [35] H.s. Kim, S. Michielsen, E. DenHartog, J. Mater. Sci. 55 (18) (2020) 7816, <https://doi.org/10.1007/s10853-020-04543-4>.
- [36] G. Glavan, M. Kurecic, U. Maver, K. Stana-Kleinschek, I. Drevenšek-Olenik, *Materials Research Express* 5 (2018) 1, <https://doi.org/10.1088/2053-1591/aaa4ec>.
- [37] Y. Li, R. Fischer, R. Zboray, P. Boillat, M. Camenzind, C. Toncelli, R.M. Rossi, *ACS Appl. Mater. Interfaces* (2020), <https://doi.org/10.1021/acsami.0c03988>.